

Intrinsic strain of defect sites steering chlorination reaction for water purification

Received: 15 July 2024

Accepted: 5 March 2025

Published online: 18 March 2025

Yinqiao Zhang^{1,5}, Mohan Chen^{1,5}, Xuanyu He¹, Erzhao Zhao², Hao Liang¹, Jingge Shang¹, Kai Liu³, Jianqiu Chen¹✉, Sijin Zuo¹✉ & Minghua Zhou⁴

Carbon nanotube (CNT)-based heterogeneous advanced oxidation processes (AOPs) used for water purification have been exploited for several decades. Many strategies for modifying CNTs have been utilized to improve their catalytic performance in remediation processes. However, the strain fields of the intrinsic defect sites on CNT steering AOPs (such as chlorination) have not yet been reported. Here, we explored the strained defect sites for steering the chlorination process for water purification. The strained defect sites with the elongated sp^2 hybridized C–C bonds boost electronic reactivity with the chlorine molecules via the initial Yeager-type adsorption. As a result, the reactive species in chlorination can be regulated on demand, such as the ratio of high-selectivity ClO^\bullet ranging from 38.8% in conventional defect-based systems to 87.5% in our strain-dominated process, which results in the generation of harmless intermediates and even deep mineralization during 2,4-DCP abatement. This work highlights the role that strain fields have on controlling the extent of chlorination reactions.

Recently, widely focused strain engineering of carbon nanotube (CNT) substrate has enabled the optimization of the physicochemical characteristics of molecular catalysts even at the sub-nanoscale; an example includes tuning the curvature of monodispersed metal phthalocyanines^{1–3}. The strain fields caused by the substrates can continuously or discretely transform the geometric and electronic layout and energy level of the metal-based overlayer to increase the catalytic activity via so-called essential interface reconstructions^{4–6}. Interface reconstructions have been customarily attained using inter-layer interactions, which involve van der Waals, π – π or donor–acceptor conjugation between the substrate and molecular catalysts^{3,7}. As such, the interface reconstructions from the substrates and catalytic center of the metal-based overlayer usually consume considerable energy in the strain fields. In addition, the contributions of the strain fields on the improvement in the reaction performances always appear to be dependent on the reaction sites. Thus, limited reactivity enhancement is usually observed^{8–10}; for example, the continuous tuning the strain of the IrO_6 octahedron in Sr_2IrO_4 slightly enhances

the oxygen evolution from 1.55 to 1.40 V overpotential at 10 mA cm^{-2} ⁹. Therefore, the strain fields on CNTs need to be efficiently utilized without useless energy consumption in the foregoing removable interface reconstruction. To the best of our knowledge, this type of design in CNT-based chemical remediation technologies for water purification has not yet been reported.

Together with these considerations, herein, we report a simple pyrolysis strategy for CNT modification to develop a set of catalysts with stable defect sites and tunable strain fields. These catalysts have been used in the mature chlorination reactions for more than a century for water purification^{11,12}, where the emerging contaminant of 2,4-dichlorophenol (2,4-DCP) as a model pollutant was abated. A series of characterizations, such as electron microscopy, spectroscopy techniques such as X-ray absorption fine structure (XAFS) spectroscopy, X-ray photoelectron spectroscopy (XPS) and electron paramagnetic resonance (EPR) were used to identify the defect sites and strain fields on the modified catalysts. Chlorination by $\text{CNT}_d\text{-S2}$ with the optimum strain for water purification was expected to overcome

¹School of Engineering, State of Key Laboratory of Natural Medicines, China Pharmaceutical University, Nanjing, PR China. ²School of Environment, Tsinghua University, Beijing, PR China. ³School of Engineering, Westlake University, Hangzhou, Zhejiang, PR China. ⁴College of Environmental Science and Engineering, Nankai University, Tianjin, PR China. ⁵These authors contributed equally: Yinqiao Zhang, Mohan Chen. ✉ e-mail: cjqer@163.com; sjzuo@cpu.edu.cn

the limitations of the high cost of UV irradiation and poor anti-disturbance performance during the conventional homogenous UV/chlorine process. Many experimental results and theoretical analyses based on density functional theory (DFT) calculations clearly revealed the important roles of the strain fields in the high-efficiency activation of chlorine and the green abatement pathway of 2,4-DCP to preliminarily respond to the aforementioned attainable expectations. Lastly, possible practical applications of this technology were confirmed by evaluating its capacity for decontaminating water.

Results

Characterizations of the CNT series

A commercial multi-walled CNT (Supplementary Fig. 3) was used as a catalyst precursor considering that it had facile defect sites and tunable strain fields¹³. The CNTs were first modified by a widely used dicyandiamide pyrolysis strategy^{14,15}; during this strategy, CNT_d (with defects), CNT_d-S1 (with defects and weak strain) and CNT_d-S2 (with defects and strong strain) were respectively obtained under increasing pyrolysis temperatures (see the Supplementary Methods for catalyst synthesis). Characterizations of high-resolution TEM (HR-TEM, Fig. 1a–c and Supplementary Fig. 4) and atomic force microscopy (AFM, Supplementary Fig. 5) intuitively revealed that the above modification process worked effectively. In detail, the HR-TEM image of CNT_d-S2 (Supplementary Fig. 4c) illustrates the evident lattice distortion in CNT_d-S2. Integrated pixel intensities of the CNT_d-S2 (Fig. 1c) from its lattice fringes (Fig. 1a) display a more distorted intensity compared with the smooth intensity on the CNT_d (Fig. 1b, c), qualitatively uncovering the above lattice distortion. In addition, compared to CNT_d, CNT_d-S2 has a larger diameter (from 15.2 to 19.4 nm, Supplementary Figs. 3, 5 and 6), higher porosity (Supplementary Fig. 7) and greater expanded *d*-spacing (0.34 to 0.36 nm, Fig. 1c). These characteristics of CNT_d-S2 were likely attributed to feasible thermo-expansion and gas evolution (such as NH₃ and NO) during the high temperature and dicyandiamide pyrolysis processes¹⁶. These factors would destabilize the *sp*² hybridized C–C bonds of CNTs, as demonstrated by the characterizations (Supplementary Fig. 8) and molecular dynamical simulations (Supplementary Fig. 9). The Raman spectra of the catalysts display three main peaks: D band, G band and 2D peak (Fig. 1d). The D band of the catalysts that usually depicts the site defects on the basal plane, displays a higher intensity for CNT_d than that of CNT, whereas the D band is nearly stable for these catalysts of CNT_d, CNT_d-S1 and CNT_d-S2 (Supplementary Fig. 10). These results indicate heavier defects on the CNT_d than on the pristine CNT but a similar degree of defects for CNT_d, CNT_d-S1 and CNT_d-S2. Moreover, high-resolution XPS spectra of C 1s on 286.15 eV binding energy assigned to the defects of catalysts (Fig. 1e) and EPR technique (Supplementary Fig. 11) for analysis of the unpaired electrons trapped by the defects of catalysts, both confirmed the above stable defects for the CNT_d series. Combining the theoretical analyses (Supplementary Fig. 12) and the conclusions from the reported works¹⁷, dual vacancy defects were potentially present in our catalysts.

Our catalysts' G band in the Raman spectra is associated with the planar stretching of *sp*²-hybridized C atoms (Fig. 1d)¹⁸. Interestingly, we clearly observed a bathochromic shift in the G band from 1592 to 1560 cm^{−1} for CNT to CNT_d-S2. The findings highlight the increased tensile strain of the CNT_d series because of the elongated *sp*² hybridized C–C bonds^{8,9}. The 2D peak of the Raman spectra, which is often related to the stretching vibration of the stacking sheet, increases in intensity in the catalysts (Fig. 1d), indicating expanded planes¹⁹. Additionally, their X-ray diffraction (XRD) patterns (Supplementary Fig. 13) demonstrate the shift of the (002) facet toward a smaller angle for the CNT_d series, further indicating expanded planes²⁰. We accordingly observed the enlarged average crystallite sizes (*L*_a) on the tube walls of the catalysts using the Debye–Scherrer equation (Fig. 1f)¹⁸. The corresponding geometric phase analysis of CNT_d-S2 (Fig. 1g) from its

HR-TEM results (Supplementary Fig. 4c) visually reveals the homogenous strain mapping on the wall²¹. Based on these observations, we conclude that the CNT_d series developed with a stable degree of defects but increased tensile strain. Electron energy-loss spectroscopy (EELS) analysis of the C K-edge in the catalysts of the CNT_d series obtained from an aberration-corrected high-angle annular dark field scanning transmission electron microscopy (AC-HAADF-STEM) displays increasingly intensity on the sharp peaks at 284.5 eV (Fig. 1h and Supplementary Fig. 14). These results indicate more excited electron transitions from the C 1s to the π^* orbital on the *sp*² hybridized C atom²⁰. Furthermore, the C K-edge near-edge XAFS (NEXAFS) spectra of the CNT_d series in Fig. 1i show the two evident peaks at 285.0 eV and −292.7 eV, which are respectively assigned to the π^* and σ^* excitations in the *sp*² hybridized C–C bond. The peak of π^* excitation increased and correlated to the complex energy transition of C 1s to π^* ²². Importantly, intensive resonance at the σ^* sites (−292.7 eV, Fig. 1i) further highlights the incremental strain in our catalysts²³. Notably, these changes in the C 1s chemical microenvironment potentially indicate improved chemical reactivity of the *sp*² hybridized C atom after strain (Fig. 2a).

Chlorination process of the CNT series

We used CNT_d series activating oxidants for the reactive species evolution to evaluate the above chemical reactivity. The fastest decay of the probe molecule via chlorine activation manifested that the chlorination process of CNT_d-S2 enabled to produce a significant number of reactive species (Supplementary Fig. 15). Thus, free chlorine utilization was further evaluated under activators of the CNT_d series. As expected, CNT_d-S2 displayed the best utilization of free chlorine (Fig. 2b and Supplementary Figs. 16, 17). Sluggish rates and nearly no catalytic kinetics were observed in CNT_d and CNT-based chlorination processes, respectively. An inveterate opinion is that defects and/or doped heteroatoms in CNT usually serve as active sites for oxidant activation^{24,25}. The contribution of defects during chlorination process was considered to be non-negligible owing to the enhanced performance from CNT to CNT_d. Considering the absence of heteroatom doping (Supplementary Figs. 14, 18 and 19) and the similar degree of defects for the CNT_d series (Fig. 1d and Supplementary Figs. 8 and 11), we attributed the above improved performance to the strain fields on our catalysts, such as the highest strain of CNT_d-S2.

The reactive species generated in the above chlorination reactions were further examined using the spectroscopy characterization and probe experiments. The DMPX signal characterized by the EPR technique using 5,5-dimethyl-1-pyrroline *n*-oxide (DMPO) as a spin-trapping agent highlighted the increased exposures of the reactive species under enhanced strain fields (Fig. 2c and Supplementary Fig. 20)²⁶. The results from the probe experiments indicated that 'OH, Cl' and ClO' were present throughout the chlorination process (Fig. 2d and Supplementary Figs. 21 and 22). The unpaired electrons of the three radicals delocalized on Cl or O atoms (Fig. 2e), and the radicals enabled the electrophilic attack; for example, the ClO' electrophilicity index of 2.15 eV was even higher than the well-known 'OH of 1.98 eV (Supplementary Table 1)^{27,28}. Other reactive species, such as singlet oxygen (¹O₂, Supplementary Fig. 23), were not detected in the present system. Interestingly, as shown in Fig. 2d, the strained catalysts could increase the exposure of reactive species by 13.2 times using the strain fields, and this value was much greater than that of the defects (only 1.7 times). Moreover, the strained catalysts could tune the distribution of reactive species, and the ratio of ClO' increased from 38.8% to 87.5%. The vital product of ClO' in chlorination was desirable for water purification because of its outstanding advantages, such as high selectivity and mild oxidation ability²⁹. These deductions clarified the highly important role of the strain fields on CNT_d than the widely reported defects alone during oxidant activation.

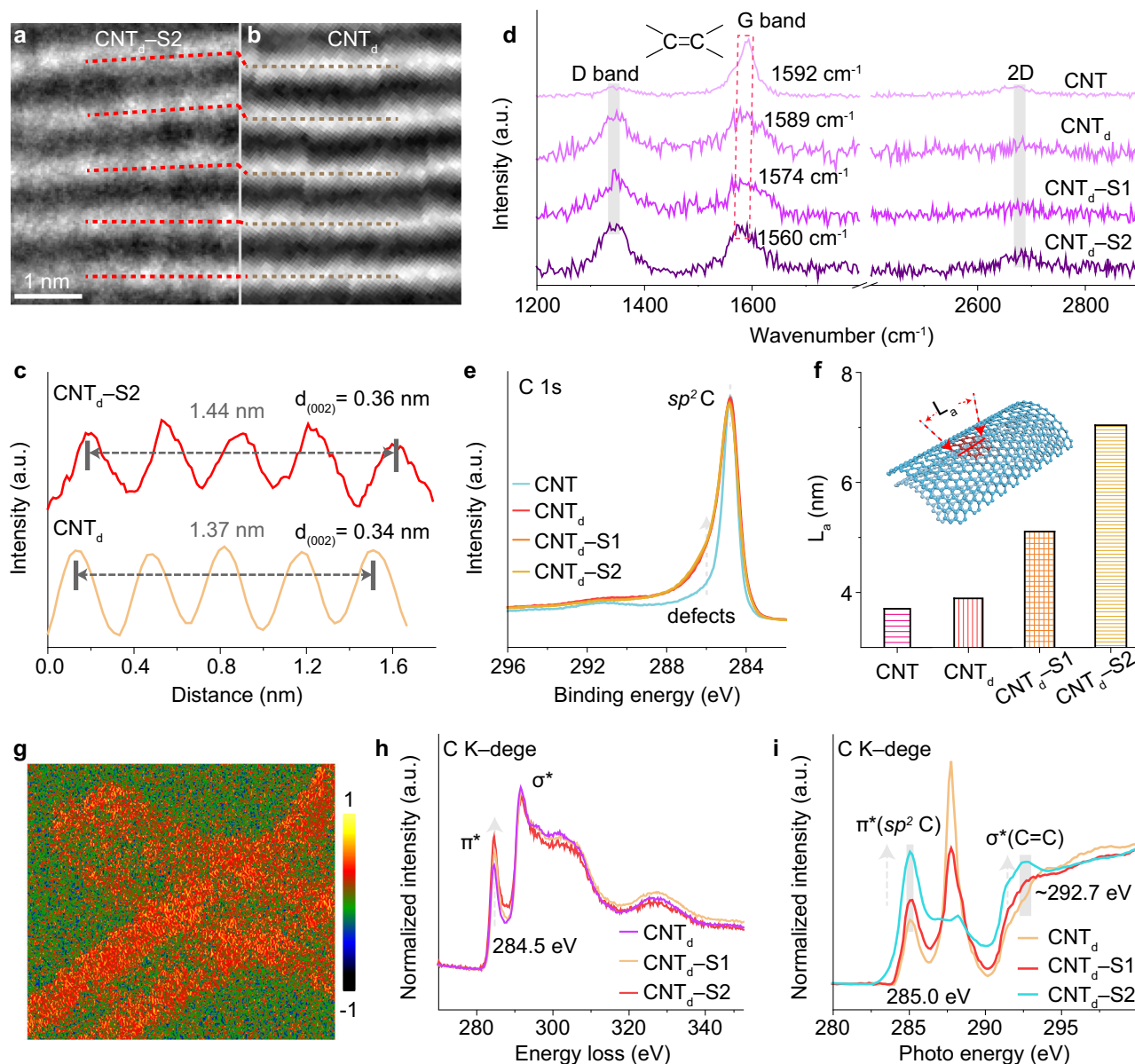


Fig. 1 | Physicochemical characterizations of the CNT_d series. Lattice fringes of (a) CNT_d-S2 and (b) CNT_d. The selected area from the HR-TEM images in Supplementary Fig. 4a, c. c Integrated pixel intensities of CNT_d-S2 and CNT_d obtained from the inverse fast Fourier transformation images in corresponding Figures (a, b), respectively. d Raman spectra of the catalysts. e High-resolution C 1s XPS

spectra of catalysts. f L_a analysis acquired from the XRD spectra of the catalysts in Supplementary Fig. 13. The inset is a schematic diagram of L_a on the tube. g Strain analysis of CNT_d-S2 obtained by geometric phase analysis from the HR-TEM images in Supplementary Fig. 4c. h HAADF-STEM EELS spectra and (i) NEXAFS spectra for the C K-edge from the CNT_d, CNT_d-S1 and CNT_d-S2 catalysts.

Chemical structures of the CNT_d series

We analyzed the electronic structures and energy band levels of the catalysts to clarify the above diverse chlorination performances. The decreased oxidation temperature from 627.1 to 587.0 °C for the strained catalysts in their differential thermogravimetry (DTG) curves (Fig. 3a and Supplementary Fig. 24) indicated that the strained catalysts had the ability of more thermodynamic-feasible electron transfer²⁰. This ability was further confirmed by electrochemical experiments based on Tafel polarization curves (Fig. 3b) and electrochemical impedance spectroscopy of the catalysts (Supplementary Fig. 25). For example, the more negative corrosion potential and larger corrosion current occurred in the Tafel polarization curves of the strained catalysts indicate more beneficial electron transfer³⁰. This likely originated from the elongated *sp*² hybridized C–C bond along with the larger spin–lattice relaxation (as demonstrated in Fig. 1) due to the metallic or semiconducting nature of CNT³¹. The electronic band

gap of the CNT_d series was then determined via ultraviolet photoemission spectroscopy (UPS, Fig. 3c and Supplementary Fig. 26). The highest occupied state (HOS), which corresponds to the highest orbital energy level of the occupied electron³², displayed an increased energy level from 0.74 eV in CNT_d to 1.20 eV in CNT_d-S2. This result indicated a downward *p* band center and increased electronic reactivity for the C atom with greater spin–lattice relaxation caused by strain³³. These changes in the electronic state induced the total energy improvement of the catalysts (Fig. 3d). Our experimental (Fig. 3c) and theoretical (Fig. 3d and Supplementary Fig. 27) results demonstrated the increased work function on the strained catalysts, and revealed the improved ability of the electron transition from the Fermi energy to the vacuum level. Additionally, the strained catalysts caused a shift their energy band structure toward Fermi energy (Fig. 3e), indicating a growing number of gap states near the Fermi energy³⁴. Therefore, the strain fields that modified the electronic state and improved the

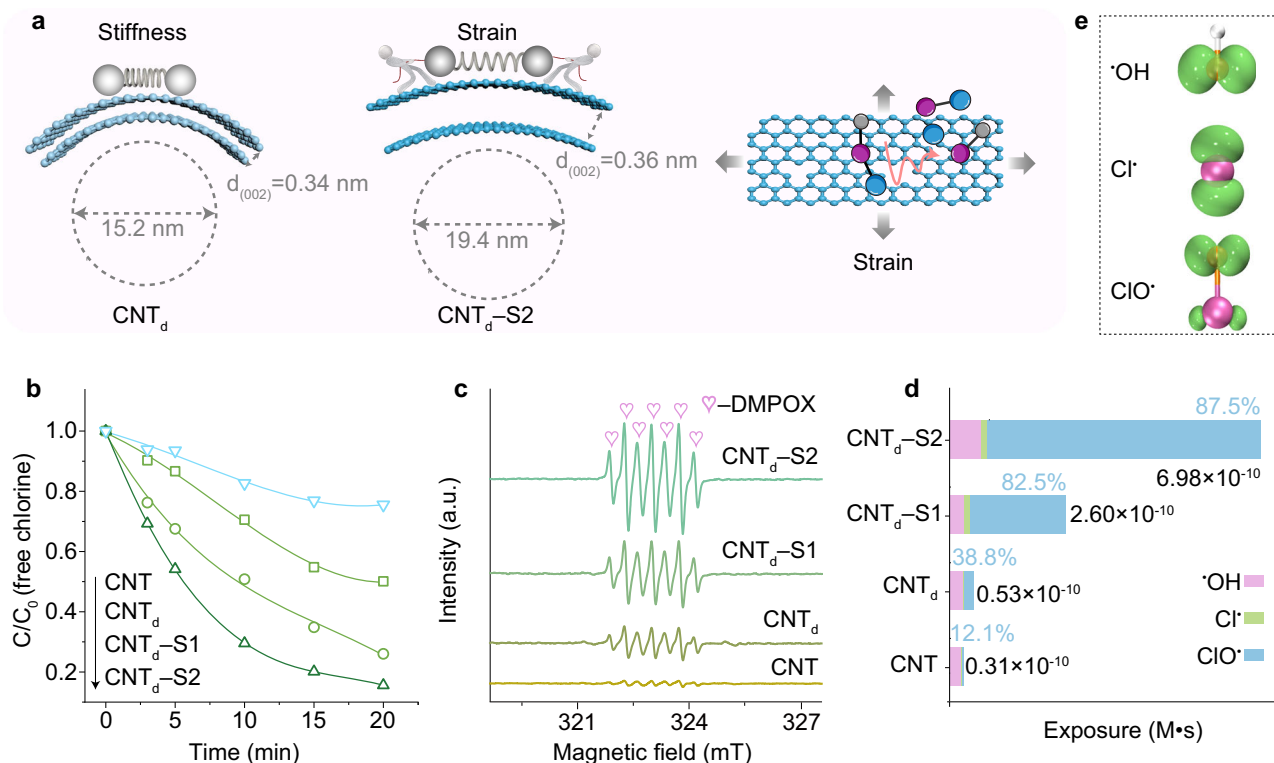


Fig. 2 | Chlorination process induced by the CNT_d series. **a** Schematic illustration of catalysts with the strain effect. **b** Time profile of the free chlorine concentration activated by our catalysts. Reaction conditions: 0.1 g L⁻¹ catalyst, 4.5 mg L⁻¹ free chlorine. **c** EPR technique using DMPO as a spin-trapping agent for the detection of

the reactive species shown in **(b)**. **d** Reactive species analysis during the chlorination process induced by our catalysts. **e** Spin density of ·OH, Cl· and ClO· from our DFT calculations.

reactivity of C atoms to boost the electron transfer with free chlorine were clearly demonstrated.

Interactive process between the CNT series and free chlorine

We subsequently investigated the evolution mechanism of the above reactive species during chlorination of the CNT_d series. The EPR test of the catalysts showed a stimulated signal intensity on the strained catalysts after they reacted with free chlorine (Fig. 4a and Supplementary Fig. 28). These results indicated that more unpaired electrons on the strained catalysts participated in the chlorination process³⁵. A set of electrochemical linear sweep voltammetry (LSV) tests for the CNT_d series in a rotating disk electrode apparatus under an inert gas atmosphere revealed enhanced electron transfer and selectivity (Supplementary Figs. 29 and 30, Fig. 4b) to quantify the above electronic conduct. For example, the electron transfer number calculated by the modified Koutecky–Levich equation (Supplementary Methods for Electrochemical experiments) was $5 \times 10^{-3} \mu\text{A rpm}^{-1}$ for the CNT_d-S2 and $2.9 \times 10^{-3} \mu\text{A rpm}^{-1}$ for the CNT_d catalyst^{36,37}. DFT calculations based on charge density difference and Bader charge analysis demonstrate an evident increase of charge transfer (1.442|e|) from the CNT_d-6% strain to hypochlorous acid (HOCl) (Fig. 4c)¹¹. The free chlorine used here was mainly HOCl based on the solution pH and its pK_a=7.5 (Supplementary Figs. 31 and 32)³⁸. In the above electrochemical process, a negative increase and a positive decrease in the current response occurred for CNT_d and CNT_d-S2, respectively, when both reacted with free chlorine (Supplementary Figs. 29a, e, and 30a, e). Both the supplementary LVS tests in a common three-electrode system (Fig. 4d and Supplementary Fig. 33) and conductivity tests of catalysts with or without free chlorine (Supplementary Fig. 34) supports these results. In contrast, almost no current change in the positive potential zone was observed (Supplementary Fig. 35). These observations emphasized the changeable electronic reduction of free chlorine via strain fields.

A plausible explanation for the above findings is that the strained catalysts likely tuned the chemisorption types of free chlorine. HOCl adsorbed on the CNT_d-0 strain and CNT_d-6% strain displayed adsorption energies of -0.264 and -1.445 eV, respectively (Fig. 4e). This difference in the adsorption energy was likely attributed to the different chemisorption types between the HOCl and CNT_d series. Our DFT calculations confirmed that the side-on Yeager-type adsorption between HOCl and CNT_d-6% strain was more thermodynamically favorable, in which both Cl and O atom were simultaneously contact with two C atoms at the strained defect sites (Supplementary Figs. 36–38, 42). However, the end-on Pauling-type adsorption between the HOCl and CNT_d-0 strain was thermodynamically feasible because of the negative adsorption energy (-0.264 eV), during which the Cl atom first contacted one C atom at a defect site (Supplementary Figs. 39–S42). In-situ Raman spectroscopy was further used to detect bond stretching during the above chlorination reactions (Supplementary Fig. 43). Two clear evolutionary peaks at approximately 660 cm^{-1} and 1015 cm^{-1} assigned to C–Cl and C–O stretching, respectively, were observed in the CNT_d-S2/free chlorine system (Fig. 4f)³⁹. In contrast, only one peak at approximately 675 cm^{-1} was observed in the CNT_d/free chlorine system (Fig. 4g). Notably, the slight redshift of the C–Cl stretching from 675 to 660 cm^{-1} after being strained again indicated intensive electronic interactions between free chlorine molecules and CNT_d-S2⁴⁰. These findings clearly showed the regulated adsorption types for free chlorine by the strained catalysts. Importantly, this regulated chemisorption conducted via our strain fields accelerated the possible rate-determining step in chlorination because the adsorption of free chlorine onto catalysts was an uphill endothermic process, according to their Gibbs free energy diagram (Fig. 4h). The subsequent heterolytic cleavage of Cl–O in free chlorine is a spontaneous exothermic process especially for CNT_d-6% strain, since the energy barrier showed a decrease from -0.912 eV for CNT_d-0 to -4.291 eV for CNT_d-6% strain. These results elucidate the

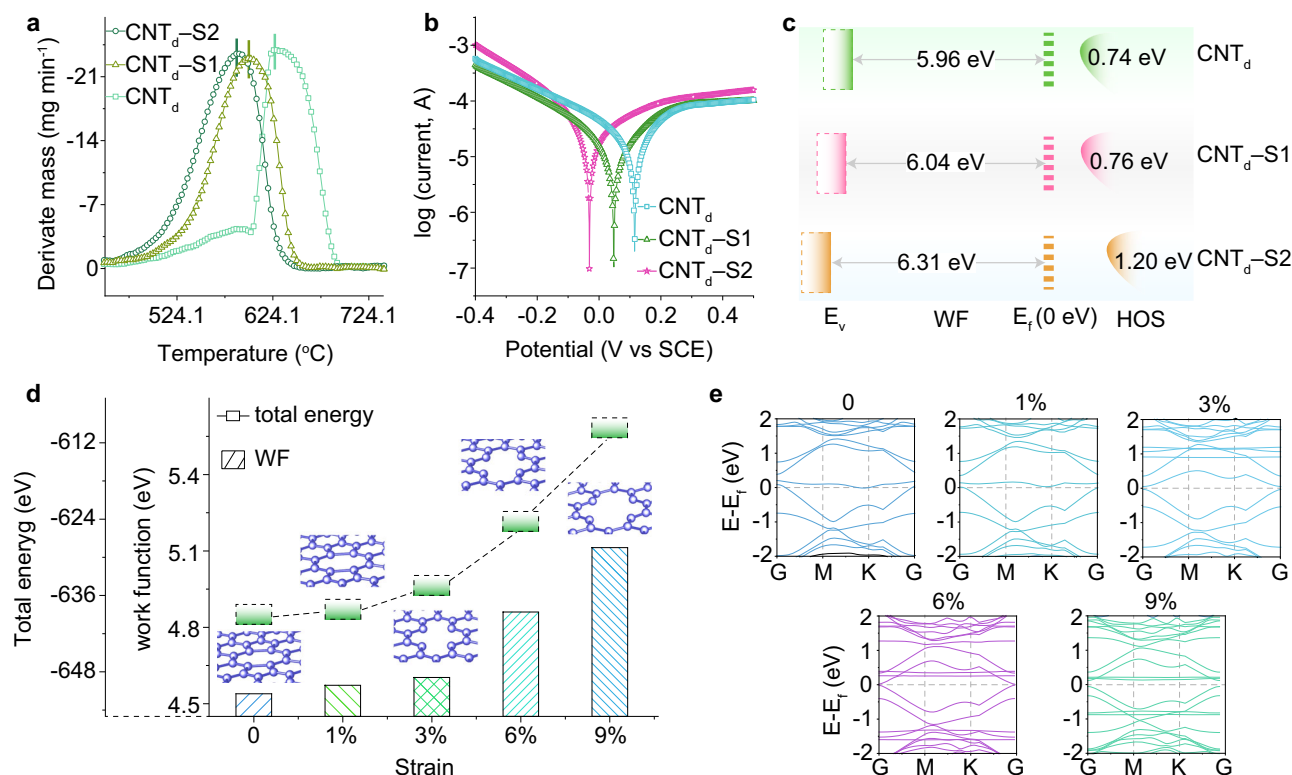


Fig. 3 | Characterizations and theoretical analysis of the electronic structure and energy band level of the CNT_d series. **a** DTG curves and **(b)** Tafel polarization curves for the CNT_d series. **c** Electronic band gap of the CNT_d series from the experimental UPS measurement. E_v Energy level of vacuum, E_f Energy level of

Fermi, HOS Highest occupied state, WF Work function. **d** Work function and total energy and **(e)** band structure of the CNT_d series obtained by the DFT calculations. The insets in **(d)** are schematic diagrams of the strained defect site.

improved adsorption and enhanced cleavage of free chlorine by our strained catalysts.

Water purification by chlorination of the CNT_d series

We applied this chlorination to water purification in view of the surging demand for clear water^{41,42}. 2,4-DCP, a widespread emerging contaminant in aqueous environments⁴³, was treated in the chlorination process. Its degradation rate after the optimized dosage of reactants (Supplementary Figs. 44 and 45) was in good accordance with the free chlorine utilization induced by the CNT_d series (Fig. 2b). For example, a slight utilization of free chlorine (Fig. 2b) along with the slow abatement of 2,4-DCP (Supplementary Fig. 45) occurred in the CNT_d-based system. In contrast, remarkable 2,4-DCP abatement was achieved in the CNT_d-S2/free chlorine system, i.e., the strain-dominated system displayed a degradation rate of 2.7 times higher than that of the defect-based chlorination process (Supplementary Fig. 45b). Notably, the strain-dominated system significantly increased the mineralization during the 2,4-DCP abatement (Fig. 5a and Supplementary Figs. 46–48). The removal of total organic carbon (TOC) was 5.0-fold greater in the CNT_d-S2-based system than that in the CNT_d-based system during 2,4-DCP mineralization (Supplementary Fig. 47). Thus, our system was superior to most reported works for 2,4-DCP mineralization (Supplementary Fig. 49). These results indicated that our strained catalysts for highly efficient utilization of free chlorine resulted in accelerated mineralization of 2,4-DCP by the C–C cleavage and did not involve the C–C or C–O coupling, as recently reported^{28,44}.

We further explored the mechanism of 2,4-DCP abatement in the present system. The results from the scavenger experiments (Supplementary Figs. 50a–c) reconfirmed that ClO[•] was responsible for 2,4-DCP abatement in the strain-dominated system (Fig. 2d), and other degradation pathways, such as ¹O₂ oxidation (Supplementary

Figs. 23 and 50d–f) or mutual activation degradation (Supplementary Fig. 51)⁴⁵, were not observed. Moreover, the electrochemical amperometric i–T curves of CNT_d-S2 showed a negative and concentration-dependent current jump after the addition of free chlorine. This phenomenon reassured the reduction of free chlorine by the foreign electron from CNT_d-S2 (see discussion in Fig. 4). Almost no fluctuation for the current after 2,4-DCP addition demonstrated that no electron transfer occurred between 2,4-DCP and the reactants. It was possibly caused by the frontier molecular orbitals of reactants and the lowest electrophilicity index for 2,4-DCP (1.18 eV, Supplementary Table 1)⁴⁶. For instance, a higher lowest unoccupied molecular orbital (LUMO) for 2,4-DCP than HOCl (Supplementary Fig. 52) indicates difficulty acquiring electrons for the former when both co-existed. Moreover, the electrostatic potential (ESP) and Fukui index mapping of 2,4-DCP further reveal the uneven charge distribution of its surface chemical sites (Supplementary Fig. 53 and Table 2). These results indicate that 2,4-DCP was vulnerable to the electrophilic, nucleophilic and radical attacks of the reactive species. Closer observation of both the ESP and Fukui indices of the 2,4-DCP molecule enables determination of the two C–Cl bonds and the single –OH group as the electrophilic sites and the three C (1 C, 3 C or 6 C) probably as the radical or the nucleophilic sites.

To verify the previously mentioned predictions, we detected the intermediates of 2,4-DCP degradation via HPLC–MS. The seven possible monomers (Supplementary Fig. 54) detected as the main products included the ortho- or para-chlorophenol (P4), ortho- or para-chlorinated dihydroxybenzenes (P3), ortho- or para-benzoquinone (P2) and chlorinated p-benzoquinone (P1). After considering the foregoing theoretical analysis of the ESP and Fukui indices, we reasoned three possible pathways of 2,4-DCP degradation, as shown in Supplementary Fig. 55. Further evaluation

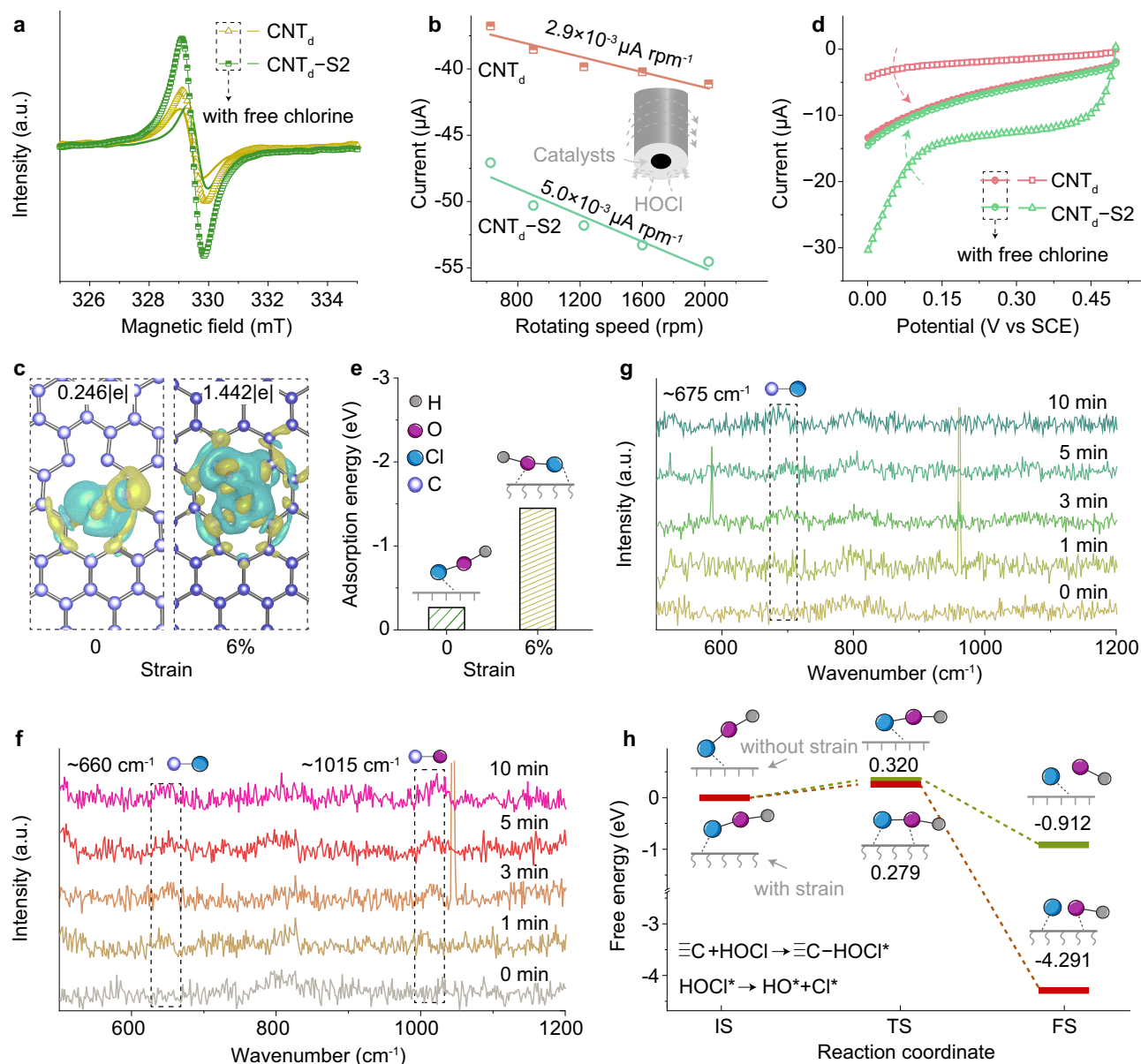


Fig. 4 | Process of electron exchange between the CNT_d series and free chlorine.

a EPR test of CNT_d and CNT_d-S2 mixed with (the solid line) or without (the hollow dots) free chlorine. **b** Modified Koutecky–Levich plot of the free chlorine reduction measured by a rotating disk electrode apparatus for CNT_d and CNT_d-S2 to estimate the electron transfer number between the catalysts and free chlorine. The inset illustrates the reaction process of HOCl and catalysts onto the electrode. **c** Charge density difference and Bader charge analysis of CNT_d without strain (0%) and with 6% strain reacting with HOCl, as calculated by DFT. The isosurfaces of green and yellow indicate the depletion and accumulation of electrons, respectively. **d** LSV

curves of CNT_d and CNT_d-S2 with (the half-hollow dots) or without (the hollow dots) free chlorine. **e** Comparison of the adsorption energy and adsorption types between CNT_d without strain (0) and with 6% strain toward free chlorine. The insets are schematic diagrams of HOCl adsorption onto the sites of the strained and unstrained. In-situ Raman spectra to detect the intermediates in **f** CNT_d/free chlorine system and **(g)** CNT_d/free chlorine system. **h** Free energy diagram of CNT_d without strain (0%) and with 6% strain used for chlorination. IS: initial state; TS: transition state; FS: final state. The insets are schematic diagrams of HOCl decomposition processes onto the sites of the strained and unstrained.

by thermodynamics and kinetics demonstrated that pathway I was more beneficial (Fig. 5c, Supplementary Figs. 56 and 57). In pathway I, 2,4-DCP first underwent a single electron transfer by a hydrogen abstract process on the -OH group to form the crucially excited 2,4-DCP* (an oxygen radical) due to the electrophilic attack of ClO[•], 'OH and Cl' (Fig. 5c inset and Supplementary Fig. 58). The excited 2,4-DCP*, which was obtained from some elemental reactions involving free-radical addition and hydrogen abstract, was then desaturated to generate chlorinated p-benzoquinone (P1). P1 was further dechlorinated to generate ortho- or para-benzoquinone (P2) by the homolytic cleavage of 4C-12Cl by ClO[•] electrophilic oxidation, considering that there is a negative change of Gibbs free

energy (ΔG) in the reaction of P1 oxidized to P2 by ClO[•] (Fig. 5c). Nevertheless, it is thermodynamically unfavorable for P2 production from P1 oxidation by 'OH or Cl' due to the positive ΔG (Fig. 5c). The minimum gap (9.15 eV) between the HOMO of P1 and the LUMO of ClO[•] also indicated the favorable oxidation of P1 by the ClO[•] (Supplementary Fig. 59). This process consumed OH⁻, decreasing the pH of the solution (Supplementary Fig. 31b). For 2,4-DCP abatement in the CNT_d/free chlorine system, six possible intermediates, including trichlorophenol and some dimers were detected (Supplementary Fig. 60). Similarly, two possible pathways of 2,4-DCP degradation were proposed (Supplementary Fig. 61). In the two pathways, the excited 2,4-DCP* (a carbon radical) was formed via single electron

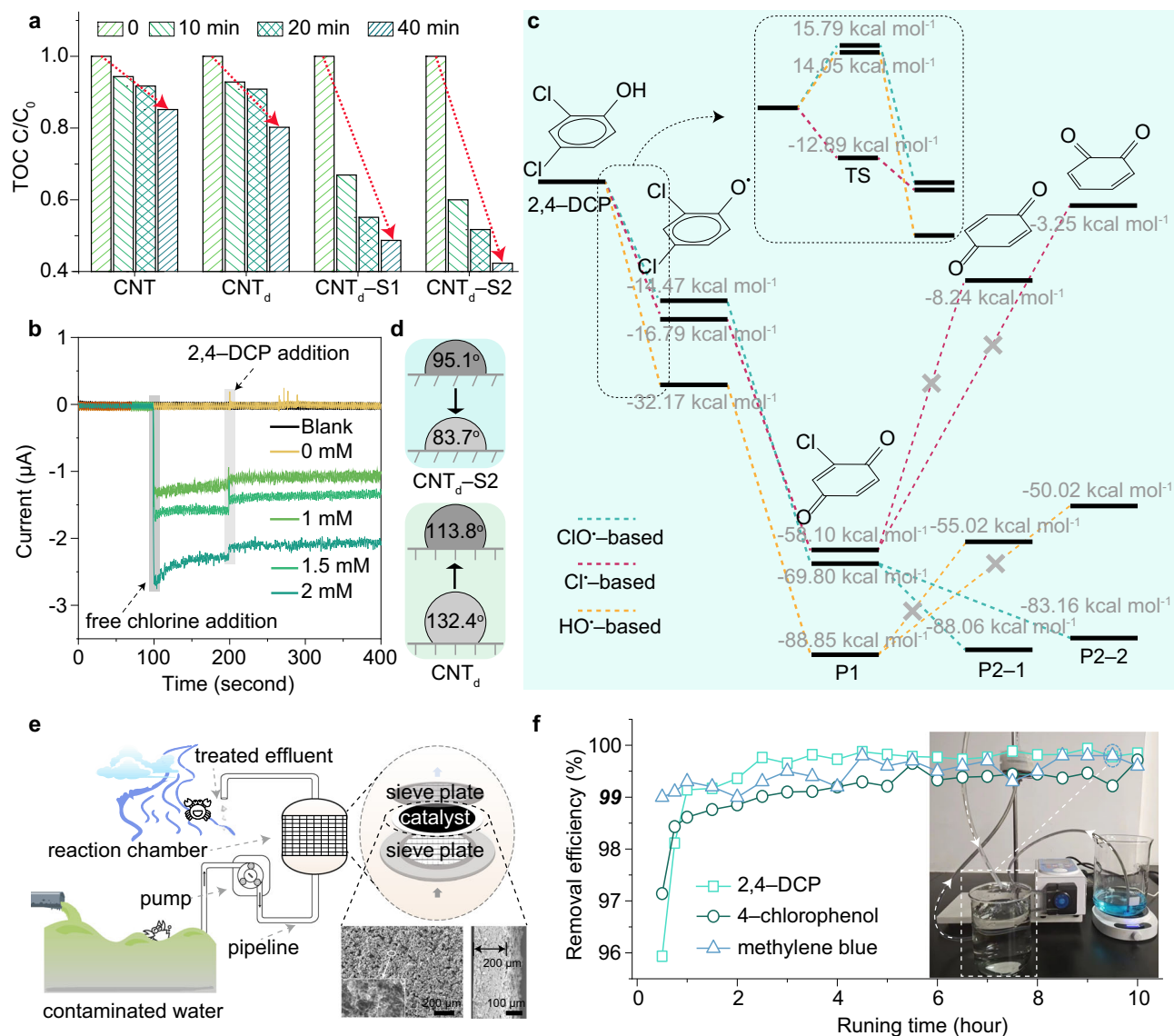


Fig. 5 | Application of the CNT_d-S2/free chlorine system for water purification.

a Time course of TOC removal in the reaction system. **b** Amperometric *i*-*t* curves of CNT_d-S2 in a three-electrode electrochemical system. Free chlorine and 10 mg L⁻¹ 2,4-DCP were added to the electrolyte at run times of approximately 100 s and 200 s, respectively. **c** Degradation pathway of 2,4-DCP in the CNT_d-S2/free chlorine system and its corresponding Gibbs free energy. The inset shows the activation energy of the transition state (TS). **d** Schematic illustration of the contact angle between CNT_d or CNT_d-S2 after contact with a solution of free chlorine alone, and a mixed solution of free chlorine and 2,4-DCP. The dark color indicates the contact angle from the catalyst in contact with the free chlorine solution. The

light color means the contact angle from the catalyst in contact with the mixed solution of free chlorine and 2,4-DCP. **e** Schematic illustration of the practical application scenario of our continuous-flow system. The SEM image of the CNT_d-S2 membrane as an inset shows a rough 200 μm height of the membrane. **f** Evaluation of the long-term operation of this continuous-flow system for the removal of 2,4-DCP, 4-chlorophenol and methylene blue. The inset displays a digital photo of the continuous-flow system where the polluted water body of methylene blue was treated and decolorized by this apparatus. The effluent was colorless. Reaction conditions: 45 mg L⁻¹ free chlorine, 10 mg L⁻¹ organic contaminants, and a 4 mL min⁻¹ flow rate.

transfer from the ·OH attack at 6 C or 1 C because Γ^0 on the two C was highly positive and ΔG was negative (Supplementary Figs. 62 and 63 and Supplementary Table 2). Subsequently, the excited 2,4-DCP^{*} underwent either self-coupling to generate P1 dimers and then generated a desaturation product of P2 via Cl[·] oxidation, or a Cl[·] addition for the production of P3. We evaluated the toxicity using the well-known Ecological Structural Activity Relationships (ECOSAR) program³⁵. A greener and simpler pathway toward 2,4-DCP degradation existed in our strain-dominated chlorination process, as outlined in Fig. 5a and c, and Supplementary Figs. 47 to 49, and 64. Unfortunately, some chlorinated products with high toxicity, such as trichlorophenol and dimers, were present in the traditional defect-based chlorination systems for the 2,4-DCP abatement

(Supplementary Fig. 64). These contrasts in the degradation pathway were mainly attributed to the high-concentration and selective reactive species and the sensitized surface energy after the 2,4-DCP addition in the strain-dominated system (Figs. 2d, 5d and Supplementary Fig. 65).

The possible practical applications of our technology were evaluated by exploring the anti-disturbance ability with respect to water matrix and long-term water remediation. On the one hand, the experimental results showed that our system could not only resist the disturbance of some common inorganic anions (such as Cl⁻, SO₄²⁻ and HCO₃⁻, Supplementary Figs. 66a–c) and typical natural organic matter (humic acid, Supplementary Fig. 66d), but also bear broad pH range (from pH 3.18 to 9.20, Supplementary Fig. 66e) and different practical

water bodies (including drinking water, tap water and surface water, Supplementary Fig. 66f and Table 3). These results highlight the crucial role of the high-selectivity ClO^\cdot and the qualified anti-disturbance ability to water matrix in future practical popularization. On the other hand, a continuous-flow reactor was constructed for the long-term treatment of contaminants. The core part of the reactor was the $\text{CNT}_d\text{-S2}$ membrane which was prepared from $\text{CNT}_d\text{-S2}$ supported on a mixed cellulose film (Fig. 5e inset and Supplementary Fig. 67a). This reactor equipped with a $\text{CNT}_d\text{-S2}$ membrane could effectively treat organics including 2,4-DCP, 4-chlorophenol and methylene blue, and had a stable degradation rate of more than 99% for long-term operation (10 hours, Fig. 5f and Supplementary Fig. 67b). The stable performance likely resulted from the robust physicochemical structure of $\text{CNT}_d\text{-S2}$ (Supplementary Fig. 68). Hence, these admirable indices indicated that our strain-dominated chlorination technique was suitable for practical applications.

Discussion

Here, we systematically illustrated the strained catalysts for the steering of the chlorination process for water purification. Stable defects and increased strain fields were produced on easily available CNT using one-step pyrolysis process. The strained catalysts have an increased energy level of HOS and an improved work function. They display the enhanced electronic activity of the C atom and then benefit the charge transport in the chlorination process. Owing to these characteristics, the strained catalysts could tune the adsorption types of free chlorine (a side-on Yeager-type adsorption) by increasing the adsorption energy, thus boosting the heterolytic cleavage of Cl-O . As a result, the strain-dominated chlorination process could result in higher exposure of reactive species and a tunable distribution of reactive species. Thus, 2,4-DCP abatement by our system displayed in faster kinetics, deeper mineralization and a greener pathway. Finally, our technology was capable of preventing disturbances in water matrix and long-term water remediation. Therefore, this technology nears the practice applications in water purification.

Despite these encouraging lab-scale results, such as the ultralow dosage of chlorine (4.5 mg L^{-1}) and the greener pathway of 2,4-DCP abatement, concerns regarding the disinfection by-products (DBPs) during the chlorination process still remain an issue for future practical applications⁴⁷. Further identifying the site-specific reactivity of the strain fields (e.g., imperfection types on tubes) for more effective chlorination and controllable evolution of reactive species is a promising alternative for mitigating DBP generation prior to large-scale real applications⁶.

Methods

Chemicals, characterizations such as Cl^- concentration (Supplementary Fig. 1), catalysts' synthesis, chlorination process involving free chlorine measurement (Supplementary Fig. 2), electrochemical test, DFT calculation method and the Supplementary Figs. and tables, etc., were recorded in the file of Supplementary Information.

Data availability

The data supporting the findings of the study are included in the main text and supplementary information files. Raw data can be obtained from the corresponding author upon request. Source data are provided with this paper.

References

- Su, J. J. et al. Strain enhances the activity of molecular electrocatalysts via carbon nanotube supports. *Nat. Catal.* **6**, 818–828 (2023).
- Fan, Y. Z. et al. Highly efficient metal-free nitrate reduction enabled by electrified membrane filtration. *Nat. Water* **2**, 684–696 (2024).
- Zhu, S. et al. Biaxially-strained phthalocyanine at poly-oxometalate@carbon nanotube heterostructure boosts oxygen reduction catalysis. *Angew. Chem. Int. Ed.* **62**, e202309545 (2023).
- Wang, L. et al. Tunable intrinsic strain in two-dimensional transition metal electrocatalysts. *Science* **363**, 870–874 (2019).
- Wang, H. T. et al. Direct and continuous strain control of catalysts with tunable battery electrode materials. *Science* **354**, 1031–1036 (2016).
- Liu, G. D. et al. Site-specific reactivity of stepped Pt surfaces driven by stress release. *Nature* **626**, 1005–1010 (2024).
- Lee, B. H. et al. Supramolecular tuning of supported metal phthalocyanine catalysts for hydrogen peroxide electrosynthesis. *Nat. Catal.* **6**, 234–243 (2023).
- Li, H. et al. Activating and optimizing MoS_2 basal planes for hydrogen evolution through the formation of strained sulphur vacancies. *Nat. Mater.* **15**, 48–53 (2016).
- Du, Y. et al. Continuous strain tuning of oxygen evolution catalysts with anisotropic thermal expansion. *Nat. Commun.* **15**, 1780 (2024).
- Yang, M. et al. Unprecedented relay catalysis of curved $\text{Fe}_1\text{-N}_4$ single-atom site for remarkably efficient $^1\text{O}_2$ generation. *ACS Catal.* **13**, 681–691 (2022).
- Kong, Q. Q. et al. Photochemical transformation of free chlorine induced by triplet state dissolved organic matter. *Environ. Sci. Technol.* **57**, 10849–10859 (2023).
- Zhao, J. et al. Multi-angle comparison of UV/chlorine, UV/monochloramine, and UV/chlorine dioxide processes for water treatment and reuse. *Water Res.* **217**, 118414 (2022).
- Yang, C. et al. Electro-driven cycling Fenton catalysis through two-dimensional electroresponsive metal-organic frameworks for water purification. *Nat. Water* **2**, 793–802 (2024).
- Miao, J. et al. Spin-state-dependent peroxymonosulfate activation of single-atom M–N moieties via a radical-free pathway. *ACS Catal.* **11**, 9569–9577 (2021).
- Shen, W. Z. et al. Activation of peracetic acid by thermally modified carbon nanotubes: Organic radicals contribution and active sites identification. *Chem. Eng. J.* **474**, 145521 (2023).
- Wei, S. J. et al. Self-carbon-thermal-reduction strategy for boosting the Fenton-like activity of single Fe-N_4 sites by carbon-defect engineering. *Nat. Commun.* **14**, 7549 (2023).
- Shao, P. H. et al. Potential difference driving electron transfer via defective carbon nanotubes toward selective oxidation of organic micropollutants. *Environ. Sci. Technol.* **54**, 8464–8472 (2020).
- Long, Y. D. et al. Tailoring the atomic-local environment of carbon nanotube tips for selective H_2O_2 electrosynthesis at high current densities. *Adv. Mater.* **35**, 2303905 (2023).
- Yu, F. B. et al. Rapid self-heating synthesis of Fe-based nanomaterial catalyst for advanced oxidation. *Nat. Commun.* **14**, 4975 (2023).
- Li, Q. et al. Shear stress triggers ultrathin-nanosheet carbon nitride assembly for photocatalytic H_2O_2 production coupled with selective alcohol oxidation. *J. Am. Chem. Soc.* **145**, 20837–20848 (2023).
- Ding, F. X. et al. Tailoring planar strain for robust structural stability in high-entropy layered sodium oxide cathode materials. *Nat. Energy* <https://doi.org/10.1038/s41560-024-01616-5> (2024).
- Pan, F. et al. Long-range ordered porous carbons produced from C_{60} . *Nature* **614**, 95–101 (2023).
- Yuan, L. et al. Modulating intrinsic defect structure of fibrous hard carbon for super-fast and high-areal sodium energy storage. *Adv. Energy Mater.* **14**, 2400125 (2024).
- Duan, X. G. et al. Insights into heterogeneous catalysis of persulfate activation on dimensional-structured nanocarbons. *ACS Catal.* **5**, 4629–4636 (2015).
- Li, N. et al. A critical review on correlating active sites, oxidative species and degradation routes with persulfate-based antibiotics oxidation. *Water Res.* **235**, 119926 (2023).

26. Cao, Y. Q. et al. Photoactivation of chlorine and its catalytic role in the formation of sulfate aerosols. *J. Am. Chem. Soc.* **146**, 1467–1475 (2024).
27. Chen, L. et al. Solar-light-activated periodate for degradation and detoxification of highly toxic 6PPD-quinone at environmental levels. *Nat. Water* **2**, 453–463 (2024).
28. Gao, X., Yang, Z. C., Zhang, W. & Pan, B. C. Carbon redirection via tunable Fenton-like reactions under nanoconfinement toward sustainable water treatment. *Nat. Commun.* **15**, 2808 (2024).
29. Guo, K. H. et al. Radical chemistry and structural relationships of PPCP degradation by UV/chlorine treatment in simulated drinking water. *Environ. Sci. Technol.* **51**, 10431–10439 (2017).
30. Li, F. et al. Efficient removal of antibiotic resistance genes through 4f-2p-3d gradient orbital coupling mediated Fenton-like redox processes. *Angew. Chem. Int. Ed.* **62**, e202313298 (2023).
31. Wang, J. H. et al. Unprecedented nonphotomediated hole (h^+) oxidation system constructed from defective carbon nanotubes and superoxides. *ACS Central. Sci.* **7**, 355–364 (2021).
32. Maiti, S. et al. Engineering electrocatalyst nanosurfaces to enrich the activity by inducing lattice strain. *Energy Environ. Sci.* **14**, 3717–3756 (2021).
33. Zhang, J. H. et al. Engineering p-band center of oxygen boosting H^+ intercalation in δ - MnO_2 for aqueous zinc ion batteries. *Angew. Chem. Int. Ed.* **62**, e202215654 (2023).
34. Hao, S. Y. et al. Torsion strained iridium oxide for efficient acidic water oxidation in proton exchange membrane electrolyzers. *Nat. Nanotechnol.* **16**, 1371–1377 (2021).
35. Zuo, S. J. et al. Decipher the key role of ketone toward singlet oxygen evolution in Fenton-like process for water decontamination. *Appl. Catal. B Environ.* **339**, 123100 (2023).
36. Song, J. S. et al. Asymmetrically coordinated CoB_3N_3 moieties for selective generation of high-valence Co-Oxo species via coupled electron-proton transfer in Fenton-like reactions. *Adv. Mater.* **35**, 2209552 (2023).
37. Yang, J. R. et al. CO_2 -mediated organocatalytic chlorine evolution under industrial conditions. *Nature* **617**, 519–523 (2023).
38. Hua, Z. C. et al. PPCP degradation and DBP formation in the solar/free chlorine system: Effects of pH and dissolved oxygen. *Water Res.* **150**, 77–85 (2019).
39. Zhang, X. T. et al. Defect rich structure activated 3D palladium catalyst for methanol oxidation reaction. *Angew. Chem. Int. Ed.* **62**, e202308968 (2023).
40. Kim, H. W. et al. Efficient hydrogen peroxide generation using reduced graphene oxide-based oxygen reduction electrocatalysts. *Nat. Catal.* **1**, 282–290 (2018).
41. Grape, E. S. et al. Removal of pharmaceutical pollutants from effluent by a plant-based metal-organic framework. *Nat. Water* **1**, 433–442 (2023).
42. Moore, M. L. et al. Moving from fit to fitness for governing water in the Anthropocene. *Nat. Water* **2**, 511–520 (2024).
43. Zhao, W., Ma, W. H., Chen, C. C., Zhao, J. C. & Shuai, Z. G. Efficient degradation of toxic organic pollutants with $Ni_2O_3/TiO_{2-x}B_x$ under visible irradiation. *J. Am. Chem. Soc.* **126**, 4782–4783 (2004).
44. Zhang, Y. J. et al. Distinguishing homogeneous advanced oxidation processes in bulk water from heterogeneous surface reactions in organic oxidation. *Proc. Natl. Acad. Sci. USA* **120**, e2302407120 (2023).
45. Xu, X. et al. Transformation of bisphenol AF during aqueous chlorination: Kinetics, mechanisms, and influence of pH. *ACS Est. Water* **1**, 449–458 (2021).
46. Kong, Q. Q. et al. The role of chlorine oxide radical ($ClO\cdot$) in the degradation of polychloro-1,3-butadienes in UV/chlorine treatment: kinetics and mechanisms. *Water Res.* **183**, 116056 (2020).
47. Mitch, W. A., Richardson, S. D., Zhang, X. R. & Gonsior, M. High-molecular-weight by-products of chlorine disinfection. *Nat. Water* **1**, 336–347 (2023).

Acknowledgements

The authors sincerely thank the financial support of the National Natural Science Foundation of China (Nos. 22306202 to S.J.Z. and 22306201 to Y.Q.Z.), the Natural Science Foundation of Jiangsu Province (No. BK20231026 to Y.Q.Z.), the Young Scientific and Technological Talents Support Project of Jiangsu Association for Science and Technology (No. JSTJ-2024-414) to S.J.Z. The authors sincerely thank Shuhan Qin from China Pharmaceutical University for beneficial assistance on molecular dynamics simulations.

Author contributions

Y.Q.Z. and S.J.Z. designed the experiment. M.H.C. and Y.Q.Z. conducted the experiment and analyzed the results. X.Y.H. and H.L. contributed to conducting TEM, in-situ Raman characterization. E.Z.Z. carried out the DFT calculation. M.H.Z., J.G.S. and K.L. provided constructive suggestions for the project. J.Q.C. proposed and supervised the project. S.J.Z. wrote and revised the paper.

Competing interests

The authors declare no competing interests.

Additional information

Supplementary information The online version contains supplementary material available at <https://doi.org/10.1038/s41467-025-57841-3>.

Correspondence and requests for materials should be addressed to Jianqiu Chen or Sijin Zuo.

Peer review information *Nature Communications* thanks Charles-François de Lannoy and the other, anonymous, reviewers for their contribution to the peer review of this work. A peer review file is available.

Reprints and permissions information is available at <http://www.nature.com/reprints>

Publisher's note Springer Nature remains neutral with regard to jurisdictional claims in published maps and institutional affiliations.

Open Access This article is licensed under a Creative Commons Attribution-NonCommercial-NoDerivatives 4.0 International License, which permits any non-commercial use, sharing, distribution and reproduction in any medium or format, as long as you give appropriate credit to the original author(s) and the source, provide a link to the Creative Commons licence, and indicate if you modified the licensed material. You do not have permission under this licence to share adapted material derived from this article or parts of it. The images or other third party material in this article are included in the article's Creative Commons licence, unless indicated otherwise in a credit line to the material. If material is not included in the article's Creative Commons licence and your intended use is not permitted by statutory regulation or exceeds the permitted use, you will need to obtain permission directly from the copyright holder. To view a copy of this licence, visit <http://creativecommons.org/licenses/by-nc-nd/4.0/>.

© The Author(s) 2025